

See discussions, stats, and author profiles for this publication at: <https://www.researchgate.net/publication/237068804>

Measurement of the Soret coefficients for a ternary hydrocarbon mixture in low gravity environment

ARTICLE *in* THE JOURNAL OF CHEMICAL PHYSICS · MAY 2013

Impact Factor: 2.95 · DOI: 10.1063/1.4802984 · Source: PubMed

CITATIONS

12

READS

64

3 AUTHORS, INCLUDING:



[Amirhossein Ahadi](#)

Ryerson University

32 PUBLICATIONS 126 CITATIONS

SEE PROFILE



[Ziad Saghir](#)

Ryerson University

225 PUBLICATIONS 1,200 CITATIONS

SEE PROFILE

Measurement of the Soret coefficients for a ternary hydrocarbon mixture in low gravity environment

Amirhossein Ahadi, S. Van Varenbergh, and M. Ziad Saghir

Citation: *J. Chem. Phys.* **138**, 204201 (2013); doi: 10.1063/1.4802984

View online: <http://dx.doi.org/10.1063/1.4802984>

View Table of Contents: <http://jcp.aip.org/resource/1/JCPSA6/v138/i20>

Published by the AIP Publishing LLC.

Additional information on J. Chem. Phys.

Journal Homepage: <http://jcp.aip.org/>

Journal Information: http://jcp.aip.org/about/about_the_journal

Top downloads: http://jcp.aip.org/features/most_downloaded

Information for Authors: <http://jcp.aip.org/authors>

ADVERTISEMENT

physicstoday

Comment on any
Physics Today article.

The image shows a red arrow pointing from the text 'Comment on any Physics Today article.' to a comment box on a sample article page. The sample article is titled 'Measured energy in Japan' by David von Seggern. The comment box contains a comment by Edger McCarroll dated 14 July 2012 19:59, discussing the energy released by a ball being hit by a bat.

Measurement of the Soret coefficients for a ternary hydrocarbon mixture in low gravity environment

Amirhossein Ahadi,¹ S. Van Varenbergh,² and M. Ziad Saghir^{1,a)}

¹*Microgravity Laboratory, Department of Mechanical and Industrial Engineering, Ryerson University, Toronto, Ontario M5B 2K3, Canada*

²*Ecole Polytechnique de Bruxelles, Université Libre de Bruxelles, Av. F.D. Roosevelt 50, 1050 Brussels, Belgium*

(Received 22 January 2013; accepted 12 April 2013; published online 28 May 2013)

While the Soret coefficients of binary mixtures have been widely measured in the past, here we report the first measurement of the Soret coefficient of a ternary mixture in a low gravity environment on board the International Space Station. The sample was contained in a 10 mm × 10 mm × 5 mm (w, l, h) cell and was monitored by means of a Mach-Zehnder interferometer at two wavelengths. The analyzed sample was a mixture of tetrahydronaphthalene, isobutylbenzene, and dodecane at the weight fraction of 0.1/0.8/0.1. While the lateral walls of the cell did not possess complete thermal isolation, the separation of the components in the central region of the cavity was comparable to purely diffusive behavior. The same experimental parameters have been monitored in Run7 and Run12 of the Selectable Optical Diagnostics Instrument-Diffusion and Soret Coefficient experiment in order to verify the accuracy of the setup. The similarity of the results demonstrates the repeatability of thermodiffusion experiments in a microgravity environment. There was nearly equal separation of the tetrahydronaphthalene and isobutylbenzene components in opposite directions, while dodecane experienced a weak separation in the same direction as isobutylbenzene. Finally, Fourier image processing and calculations of the transient separation of the components were used to analyze the heat transfer in the system and to measure the Soret coefficients for this ternary mixture. The successful measurements shown in this work can serve as the standard for ground experiments and for numerical modeling of hydrocarbon mixtures. © 2013 AIP Publishing LLC. [<http://dx.doi.org/10.1063/1.4802984>]

I. INTRODUCTION

Thermodiffusion, also called the Soret effect, is a phenomenon involving heat and mass transfer in a solid, liquid, or gas due to a temperature gradient. It is important in oil exploration and in optimal oil recovery since it causes diffusion fluxes in hydrocarbon reservoirs. Oil exploration models are being developed to simulate these phenomena over several centuries, and improved oil recovery models are also being developed to estimate and locate different compositions in oil reservoirs.^{1–4} Soret coefficient values are usually ignored in most engineering applications; however, an accurate and advanced modeling of mass diffusion is critical for this kind of oil recovery investigation. This phenomenon is more pronounced in oil fields, usually due to the porous environment.^{5,6} The Soret coefficient is recognized as difficult to determine at ground conditions because of technical constraints in the control of liquid convection and convective instabilities for most of the mixtures.^{7–9} However, measurements conducted in a controlled microgravity environment minimize the perturbation effects of gravity and allow the true diffusion limit to be achieved. A microgravity environment provides a unique tool for studying the behavior of liquids and measuring transport coefficients.

There are several experimental techniques to investigate the Soret effect, such as the thermogravitational

column,^{10–15} diffusion cell,¹⁶ thermal flow field fractionation, light scattering,^{17,18} thermodiffusion-forced Rayleigh scattering,^{19–22} laser beam deflection,^{23,24} and holographic interferometry.^{25–31} But these techniques and the development of theoretical models have been mainly performed for binary mixtures.^{3,4,32} On the other hand, there is a scarcity of experimental investigations on ternary mixtures. In fact, the performances of the current models weaken as the number of components in the mixture increases.³³ This gap of ternary and multi-component data has initiated the improvement of the current multi-component thermodiffusion models. Efficient measurement of the thermodiffusion coefficients and molecular diffusion coefficients in the convection-free regime is the main method for accurately testing different theoretical models.^{4,32} Accordingly, in this study we had to verify the accuracy of the experimental methods that were used to measure the coefficients in order to have the results be useful for the further development of ternary or multi-component models.

The SODI (Selectable Optical Diagnostics Instrument) experiment was implemented under the overall supervision of NASA and the ESA. The main purpose of the DSC (Diffusion and Soret Coefficient) project was the measurement of diffusion coefficients of selected ternary mixtures, taking advantage of the reduced gravity environment available on board the International Space Station (ISS).^{38,39} Combinations of complementary techniques were used to characterize flight candidate samples consisting of both water-based

^{a)}Email: zsaghir@ryerson.ca

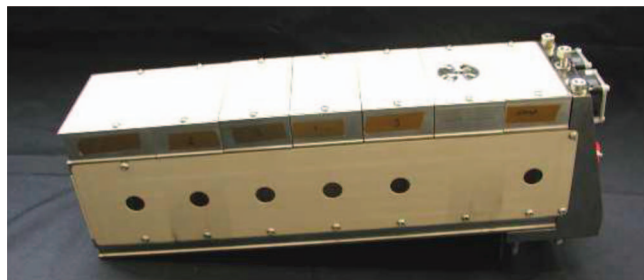


FIG. 1. Front view of the DSC cell array.⁴⁹

and hydrocarbon mixtures. Experimental results from space experiments performed using the SODI facilities have been used to test thermodiffusion theories and develop physical and mathematical models for the estimation of thermodiffusion and diffusion coefficients.³⁹ Different cell arrays were planned in the SODI project. Figure 1, shows DSC cell array which included six cells for the last series of experiments on board the ISS. Accordingly, it was expected that this experiment would deliver high precision benchmark measurements on scientifically and industrially relevant multi-component mixtures. Consequently, the main aims of this new diffusion project on board the ISS were first to develop and implement techniques for the measurement of diffusion and thermodiffusion coefficients in ternary mixtures on the ground, second to apply such techniques for the selection of relevant liquid mixtures for the space experiments, third to measure diffusion and thermodiffusion coefficients of selected mixtures on board the ISS, and finally to retrieve and analyze data from the microgravity experiment and compare them with experimental results obtained on the ground in order to validate and extend existing theoretical and numerical models for heat and mass transport.³⁹ The sample was contained in a 10 mm \times 10 mm \times 5 mm (w, l, h) cell and monitored by a Mach-Zehnder interferometer. Mixtures of tetrahydronaphthalene-isobutylbenzene-dodecane (THN-IBB-C₁₂) at five different compositions were hosted in the DSC cell array.

Shevtsova has investigated the kinetic mechanisms that drive diffusion as well as the effects of g-jitter on the molecular diffusion and thermodiffusion processes.^{27,28,31,40,41} The thermal simulation of thermodiffusion in ternary hydrocarbon mixtures at high pressure was investigated by Srinivasan *et al.*⁷ They have used the special formulation of the Firoozabadi model⁴² to calculate the net heat of transport in the molar average velocity frame. The thermodiffusion model has been coupled with the PR-EOS (Peng-Robinson Equation of State) and has been validated against experimental results.^{17,30} An experimental study of thermovibrational convection in the low gravity condition was performed by Mialdun and Shevtsova.³⁰ They studied this configuration at both weightless and ground conditions theoretically and experimentally. The observed convection patterns were the first direct experimental evidence of thermovibrational convection in low gravity as a result of vibration of non-uniformly heated fluid.^{35–37,43} The behavior of thermo-solutal diffusion in high pressure liquid mixtures in the presence of vibrations were investigated numerically for binary and ternary mixtures.^{9,44,45} The separation direction of the species with an intermediate

molecular weight at low concentration was toward the hot side, while at higher concentrations it diffused to the cold side.

Five different ternary hydrocarbon mixtures of methane, *n*-butane, and *n*-dodecane have previously been studied in a microgravity environment. The experiments on board the satellite FOTON-M3 were analyzed in a specially designed apparatus.⁴⁶ The mixture was kept at a pressure of 35 MPa to ensure that methane was in the liquid state throughout the experiment. It was found that in all mixtures methane and *n*-dodecane separated to the hot and cold sides, respectively. *N*-butane, at low concentrations, separated to the hot side; however, at higher concentrations it diffused to the cold side. This sign change is explained by the intermediate density of *n*-butane and its interaction with methane. Computational investigations were made in which a thermodiffusion model based on the theory of irreversible thermodynamics was applied to these ternary mixtures. It was shown that the model performed well only for certain compositions. That is, the sign change behavior of *n*-butane was not accurately captured.⁴⁶

A correlation of the net heat of transport, defined in non-equilibrium thermodynamics, with the activation energy of viscous flow was done to obtain an expression for the thermodiffusion factor of a liquid mixture. In the linear, non-equilibrium thermodynamics approach, an expression was derived to calculate the thermodiffusion coefficients for ternary mixtures. These estimates matched with the experimental data.⁴

Another set of studies tested the performance of the SODI apparatus using the configuration and cell array of the DSC experiment. While the cell was monitored only with one wavelength instead of two, valuable information about the instrument performance was gained. The thermal design of the microgravity cell was found not to be optimized for ground experiments, but it exhibited promising performance in a zero gravity environment.⁴⁷

The Soret coefficients, the thermodiffusion coefficients, and the isothermal mass diffusion coefficients of the three binary systems of mixtures of THN, IBB, and C₁₂ within the framework of an international benchmark test have been measured.^{17,48} Final coefficients resulting from these mixtures were in good agreement with those obtained by other benchmark tests. The maximum deviation for the Soret coefficient from the proposed benchmark values was only 7%. It proved that reliable data may be obtained using convective coupling, instead of trying to avoid convection by using a microgravity environment.^{17,48} In a similar work, the Soret, diffusion, and thermodiffusion coefficients of the three binary mixtures of dodecane, isobutylbenzene, and 1,2,3,4-tetrahydronaphthalene for different compositions at a mean temperature of 298 °C were measured.¹¹ The authors provide a detailed analysis of the measurement process of the beam deflection cell, which allowed an elegant extension to include temperature gradients within the cell. In addition, ethanol-water mixtures were investigated precisely over a broad concentration and temperature range. Generally, good agreement between this measurement and the literature data was achieved, with improved values for the diffusion coefficient in the range where the Soret coefficient changes its sign.²⁴

Recently, the beam deflection technique was employed to measure diffusion and thermodiffusion in ternary fluid mixtures.²³ A highly sensitive two-color beam deflection setup made it possible to determine the time-dependent concentration profiles of all three components. By comparing the measured beam deflection signals to a numerical solution of the coupled heat and mass transport equations, the diffusion matrix, the thermodiffusion coefficients, and the Soret coefficients were found by a numerical model combined with a nonlinear least-squares fitting routine. It was found that results could be improved by additional thermodiffusion forced Rayleigh scattering experiments, which produced a contrast-weighted average thermodiffusion coefficient.²³

The thermodiffusion coefficients of six hydrocarbon liquid ternary mixtures at 25 °C using the thermogravitational technique have been measured by Bou-Ali and his team. These mixtures consisted of different mass fractions of THN-IBB- C_{12} at four different concentrations, and 1,2,3,4-tetrahydronaphthalene-isobutylbenzene and *n*-decane at two concentrations.¹⁴ The authors proposed a new model that accurately predicts the data within the experimental error bar. The improvement lies in the use of a plane column with a smaller gap dimension than those used previously. Differences smaller than 4% have been found between the data measured in this work and the cylindrical column.¹⁴

The present paper reports results for the second cell of the DSC array filled with a ternary mixture of THN-IBB- C_{12} at a weight fraction of 0.1/0.8/0.1. Two experiments, named Run7 and Run12 according to the SODI-DSC timetable, that possessed mean temperatures of 298 K were investigated in this work. The extracted data were the refractive index variations in the cavity caused by temperature and concentration differences and were obtained by processing the recorded images using different Fourier transform and phase shifting methods. Eventually, the Soret coefficients were obtained either by assuming the system had reached the steady state or by curve fitting using a genetic algorithm. The similarity between the results obtained by the two methods show that the experimental runs were long enough to reach a steady state of Soret separation for all the components. While perfect thermal isolation near the lateral walls was not obtained, separation of the components in the mixture was measured in the middle of the cavity, a region in which the mixture behaved purely diffusively. Section II explains the optical setup and Sec. III presents the experimental procedure. Sections IV and V present, in detail, the mathematical approach used to extract information from the raw images. Results and discussion are presented in Sec. VI, and in Sec. VII, a summary of this study is provided.

II. OPTICAL EQUIPMENT TO MEASURE S_T ON BOARD THE ISS

The SODI facility has been designed to provide a variety of fluid experiments with precise thermal control and high-quality optical diagnostics. The main feature of the SODI design is to have a modular instrument for operation in the MSG (Microgravity Science Glovebox), shown in Fig. 2. SODI is equipped with various optical diagnostics, such as a Mach-Zehnder interferometer, particle image velocimetry, and near



FIG. 2. SODI facility and CSA astronaut Bob Thirsk, on-board ISS before installing DSC cell array inside that box.⁵⁷



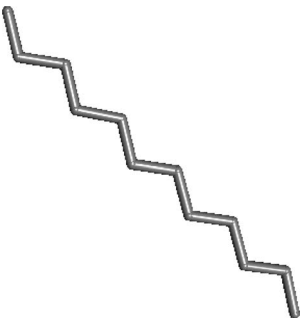
field scattering techniques. Each particular experiment is provided its own dedicated array of experimental cells, which are mounted into the SODI facility by an astronaut. In the modular approach, where the experiment module is the central element, it is possible to change some parts of the SODI without any significant disruption to the diagnostic instruments or having to remove the facility from the MSG. For example, switching from one experiment to another requires only changing the experimental cells or cell arrays shown in Fig. 1. The mixture components have been chosen because they are representative of a hydrocarbon reservoir mixture.³⁴ THN represents the family of naphthenic compounds, while IBB represents the aromatic compounds, and finally C_{12} represents the aliphatic compounds. The chemical structures, properties, and their molecular shapes are provided in Table I. The selection of these fluids depended on two parameters: first, the ground-based experimental results, and second, the feasibility of being investigated using SODI and of data analysis.

Figures 3(a) and 4(a) show the actual apparatus and schematic setup, respectively, of the optical digital interferometry (ODI) instrument, while Figs. 3(b) and 4(b) illustrate the experimental and schematic setup, respectively, of the particle image velocimetry experiment used in this experiment. A detailed description of the optics contained in the different modules is given in the optical design report.⁴⁹

The cell arrays were designed first to contain the sample cells, allow their exchange within the SODI facility, and keep them aligned with the optical modules, and second to provide thermal control to the sample cells during the experiment. Five different compositions of the THN-IBB- C_{12} mixture were loaded in the first cell array of DSC; while, the second cell array was filled with different compositions of mixtures of cyclohexane-toluene-methanol.

The last parts of Figs. 3 and 4 show the assembled apparatus, which consists of three parts: An interferometric system in combination with equipment for digitally recording the phase information, the diffusion cells, and the temperature controller units. Figure 5 shows the cell design and the scheme of the thermal regulation system. There are two

TABLE I. Chemical properties of three components of SODI-DSC test mixtures.

EPA substance registry system	1,2,3,4-tetrahydronaphthalene	Isobutyl benzene	n-dodecane
Abbreviation name	THN	IBB	C ₁₂
Molecular formula	C ₁₀ H ₁₂	C ₁₀ H ₁₄	C ₁₂ H ₂₆
Molecular structure			
Density at 298 K (g/cm ³)	0.971	0.850	0.747
Molecular mass (g/mol)	132.21	134.22	170.34

PID (proportional-integral-derivative controller) temperature controllers to regulate the temperature at the lower and upper sides of the cells. These two regions are covered by two copper blocks that provide a consistent temperature to the side of the cell as because of their high thermal conductivity.

The cell configuration was selected based on an optimization analysis of different aspect ratios of the Soret cell, and it was made of Suprasil quartz.^{28,37} Mialdun and Shevtsova³¹ optimized the cell size and shape and showed the importance of the thermal design in their recent work. The cells used in the SODI experiments were supposed to avoid heat transfer between various sides of the cell and environment. There should be a particular cell size that reduces convection inside the cell and provides a linear temperature distribution inside the test liquid. However, according to our results, this goal was not completely achieved.

III. EXPERIMENTAL PROCEDURE

The sample was monitored using a Mach-Zehnder interferometer with two lasers of constant frequency at wavelengths $\lambda = 670$ nm and $\lambda = 935$ nm. The beams were expanded by a spatial filter and then passed through a beam splitter. One of the beams then traveled through the cell holder and the experimental cell while the other bypassed the cell and was used as reference. Figures 4(a) and 4(b) show the two different paths inside the cell holder. One of the paths passed through the front of the cell (in the direction perpendicular to the thermal gradient) and the other one passed through the void area to be used as the reference beam. After passing mirrors, the two beams interfered with each other at a second beam splitter. Finally, interference fringes were captured by the Pantera SA 2M30CCD camera (Charge Coupled Device), manufactured by Dalsa.

The first step to a measurement was thermalization of the sample at the mean temperature to initialize the mixture characteristics by reaching uniform concentration and tempera-

ture inside the cavity. The mean temperature that was established at the top and bottom plates of the cell was 25 °C for half of the DSC experimental runs (which were considered in this study) and 40 °C for the other half. During the first 90 s of this phase, no images were acquired. This step was performed while the experimental run on the previous cell was still being performed in order to reduce experiment duration. Then the temperature gradient was established, from 6 to 8 h depending on whether the run was normal or extended, respectively. The temperature field reached thermal stability within 3 min (first thermal time) from the imposition of the temperature difference. ODI images and the Peltier elements' temperature corresponding to this phase were acquired. It must be noted that at the beginning of the experiment one image was recorded every 3 s. As time passed, the time step between recorded images was increased to the maximum time step of 180 s. After thermodiffusion was completed, the temperature difference was removed, and the cell was brought back to the mean temperature within 3 min (second thermal time). The data for the active cell were then acquired for 4–6 h. After each run, the system was brought to the initial isothermal and homogeneous concentration conditions. If needed, the run was repeated at a different temperature difference. After the experiment was finished, the moveable optic bridge was moved to the next sample and the cycle was repeated.

Thermal equilibrium is established at a characteristic time that is a function of the length of the experimental cell and the thermal diffusivity of the liquid mixture $\tau_{th} \propto L^2/\chi$. During this period, the influence of diffusion due to thermal gradients on the refractive index is negligible because the effect of the thermal contrast factor is two orders of magnitude larger than that of the concentration contrast factor.³¹ Thus, any change in the refractive index in this period was assumed to be due to temperature. Eventually, a concentration gradient was established by continuing to impose the temperature differential across the experimental cell. There

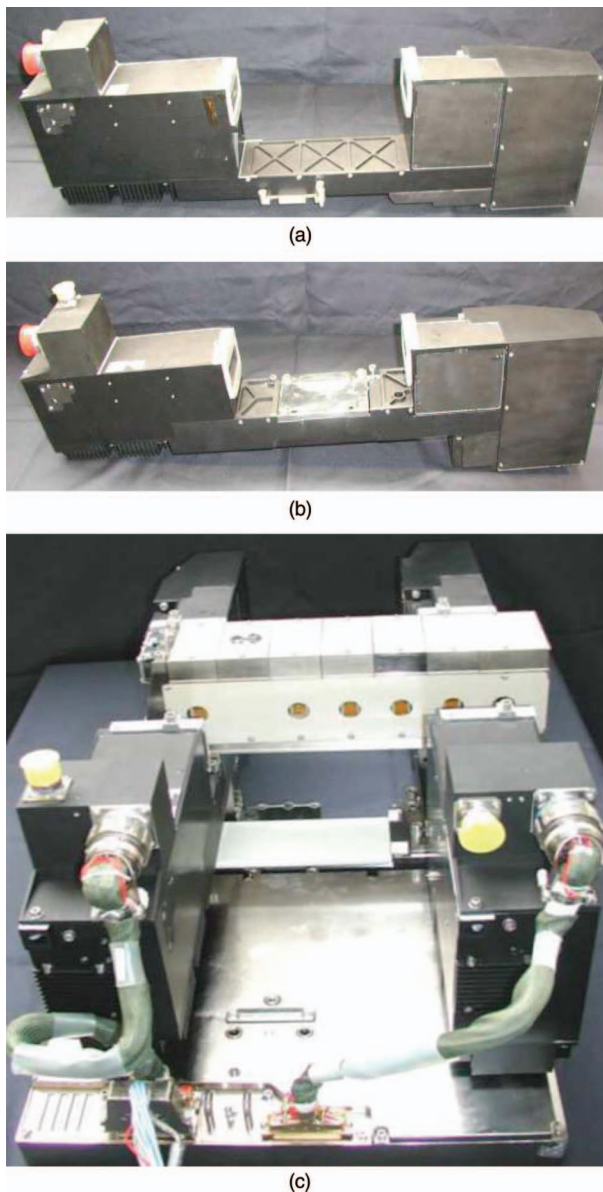


FIG. 3. (a) Interferometer moving bridge, (b) interferometer fixed bridge, and (c) assembled SODI-DSC experimental apparatus.⁴⁹

was a characteristic diffusion time that is similar to the thermal time as it is also a function of the cell length: $\tau_C \propto L^2/D$, where D is the smallest eigenvalue of the diffusion matrix. By definition, at the end of the diffusion time the linear separation of species has been reached. Although the assigned period for thermodiffusion time was not long enough for a mixture of water-isopropanol to reach steady state (during the first series of SODI experiment on board ISS),^{27,28} the diffusion time in this series of experiments was enough, as shown in Fig. 6. The separation of the alcohol mixtures showed a noticeable separation and slope of concentration variation at the end of the thermodiffusion step. However, Fig. 6 demonstrates small, intense fluctuations during the last two hours of the separation phase caused by technical errors in the optical measurement and it seems that the steady separation is reached.

IV. MATHEMATICAL APPROACH TO EXTRACT Soret COEFFICIENTS

The diffusive mass transport in a ternary mixture in the presence of a temperature gradient is described by three fluxes: one as a result of the temperature difference and two independent mass fluxes. There is no need to define the third mass flux for the last component because the final closing relation describes the third mass flux completely. Given, $i = 1, 2$, and 3 , the mass fluxes along the direction of the thermal gradient are given by Eqs. (1)–(3)

$$\vec{J}_1 = \rho(-D_{11}\nabla c_1 - D_{12}\nabla c_2 - D_{T1}c_1(c_2 + c_3)\nabla T), \quad (1)$$

$$\vec{J}_2 = \rho(-D_{21}\nabla c_1 - D_{22}\nabla c_2 - D_{T2}c_2(c_3 + c_1)\nabla T), \quad (2)$$

$$\sum_{i=1}^3 \vec{J}_i = 0, \quad (3)$$

where ρ is the density of the mixture, c_i is the mass fraction of the i th component, D_{ii} is the pure diffusion coefficients, with $i \neq j$ the cross diffusion coefficients, and $D_{T,i}$ represents the thermodiffusion coefficients of the i th components in the ternary mixture. Mass conservation equations, with previous phenomenological equations and the assumption of no convection, allow writing the following equations that govern the time evolution of the component concentration along the thermal gradient:

$$\frac{\partial c_1}{\partial t} = \rho(D_{11}\nabla^2 c_1 + D_{12}\nabla^2 c_2 + D_{T1}c_1(c_2 + c_3)\nabla^2 T), \quad (4)$$

$$\frac{\partial c_2}{\partial t} = \rho(D_{21}\nabla^2 c_1 + D_{22}\nabla^2 c_2 + D_{T2}c_2(c_3 + c_1)\nabla^2 T), \quad (5)$$

$$\sum_{i=1}^3 \frac{\partial c_i}{\partial t} = 0. \quad (6)$$

As the cross-diffusion coefficients are negligible in comparison with the pure diffusion coefficients, and the linear thermal gradient is established rapidly. Thus, the concentration difference between the hot and cold sides of each component can be simplified and solved as a function of time, as given below

$$\Delta C_1(t) = C_1(t, L) - C_1(t, 0) = S_{T1}c_1(c_2 + c_3)\Delta T \times \left[1 - \frac{8}{\pi^2} \sum_{n, \text{odd}} \frac{1}{n^2} \exp\left(-n^2 \frac{t}{\tau_{D11}}\right) \right], \quad (7)$$

$$\Delta C_2(t) = C_2(t, L) - C_2(t, 0) = S_{T2}c_2(c_3 + c_1)\Delta T \times \left[1 - \frac{8}{\pi^2} \sum_{n, \text{odd}} \frac{1}{n^2} \exp\left(-n^2 \frac{t}{\tau_{D22}}\right) \right], \quad (8)$$

$$\sum_{i=1}^3 C_i = 1, \quad (9)$$

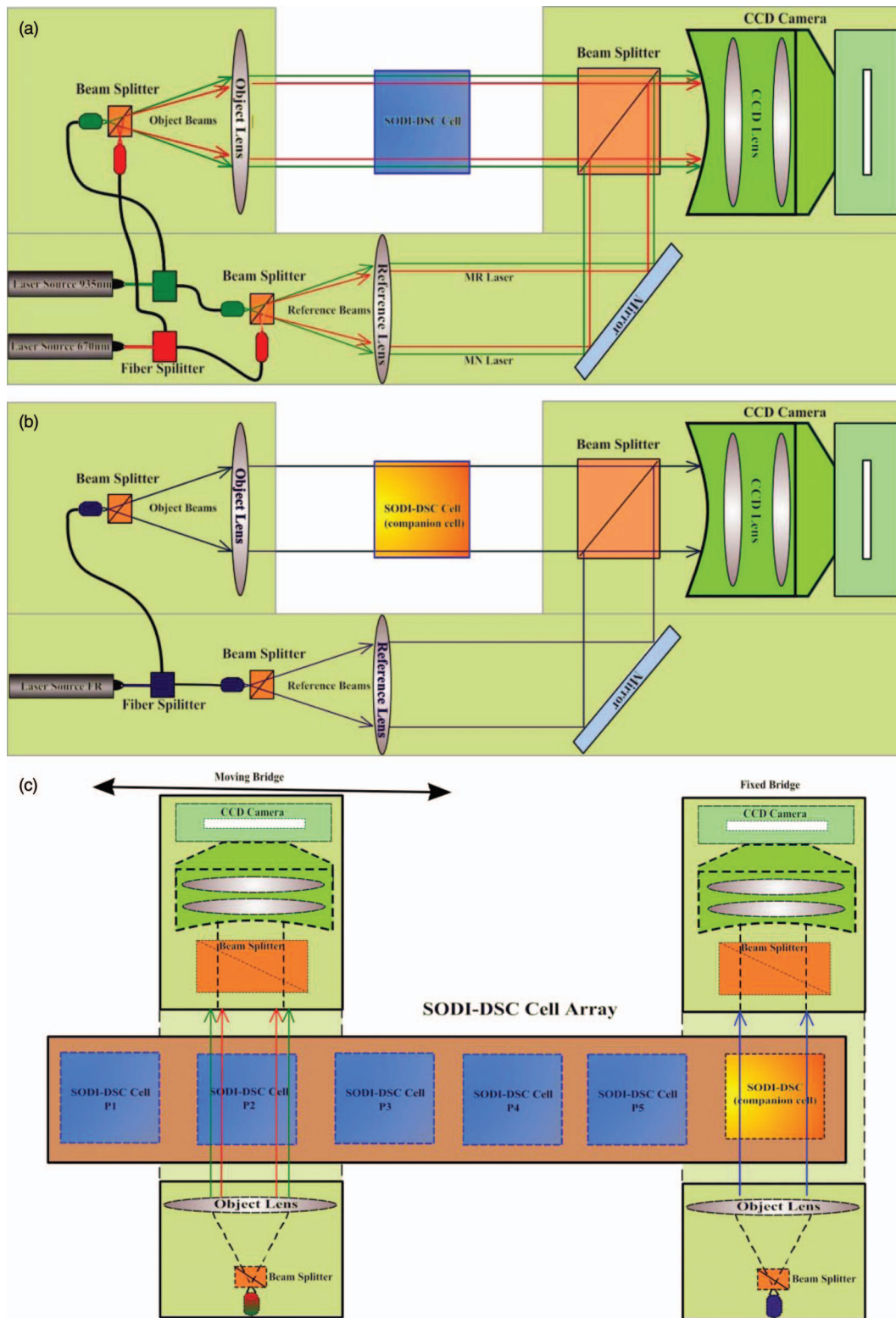
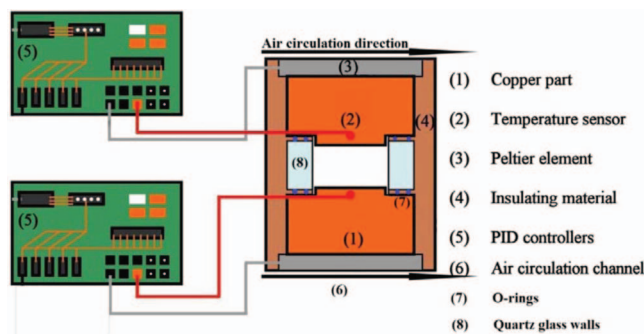


FIG. 4. (a) Scheme of the interferometer moving bridge setup, (b) scheme of the interferometer fixed bridge setup, and (c) assembled SODI-DSC scheme of experimental setup.

where $\tau_{D_{11}} = L^2/\pi^2 D_{11}$, $\tau_{D_{22}} = L^2/\pi^2 D_{22}$, and L is the distance between the hot and cold sides of the diffusion cell. $S_{T1} = D_{T1}/D_{11}$ and $S_{T2} = D_{T2}/D_{22}$ represent the Soret coefficients of the ternary mixture, and S_{T3} is defined from the concentration variation of the third component. Using only one laser source provides one equation, as below, that has two

unknowns during the diffusion time, ΔC_1 and ΔC_2

$$\Delta n_1(x, y) = \left(\frac{\partial n_1}{\partial T} \right)_{T_0, C_0, \lambda_1} \Delta T(x, y) + \left(\frac{\partial n_1}{\partial c_1} \right)_{T_0, C_2, \lambda_1} \times \Delta C_1(x, y) + \left(\frac{\partial n_1}{\partial c_2} \right)_{T_0, C_1, \lambda_1} \Delta C_2(x, y), \quad (10)$$

FIG. 5. Experimental cell and temperature controller sketch.⁵⁸

where $\Delta T(x, y)$ and $\Delta C_1(x, y)$ are the temperature and concentration changes at the point (x, y) , respectively. $(\partial n / \partial T)$, which is generally two orders of magnitude smaller than the concentration contrast factor, is the variation of the refractive index due to temperature, and $(\partial n / \partial c)$ is the variation of the refractive index due to concentration. For instance, $(\partial n_2 / \partial c_1)_{p_0, T_0, C_3, \lambda_2}$ means the rate of change of the refractive index with a change in the concentration of the first component in the condition of initial pressure, temperature, and constant mass fraction of the third component while the second laser is being used. The contrast factors are functions of both composition and temperature; however, because only small changes occur in these parameters, these coefficients are assumed constant for each specific mixture and are taken from the literature^{29,30,36} based on the mean temperature of the mixture. To make the equations solvable, a second laser source of different wavelength with specific kinetics for each wavelength was used in the experiment. This addition makes it possible to obtain ΔC_1 and ΔC_2 using Eq. (10). It is noted that ΔC in this paper represents the maximum separation between the hot and cold sides

$$\Delta n_2(x, y) = \left(\frac{\partial n_2}{\partial T} \right)_{T_0, C_0, \lambda_2} \Delta T(x, y) + \left(\frac{\partial n_2}{\partial c_1} \right)_{T_0, C_2, \lambda_2} \times \Delta C_1(x, y) + \left(\frac{\partial n_2}{\partial c_2} \right)_{T_0, C_1, \lambda_2} \Delta C_2(x, y). \quad (11)$$

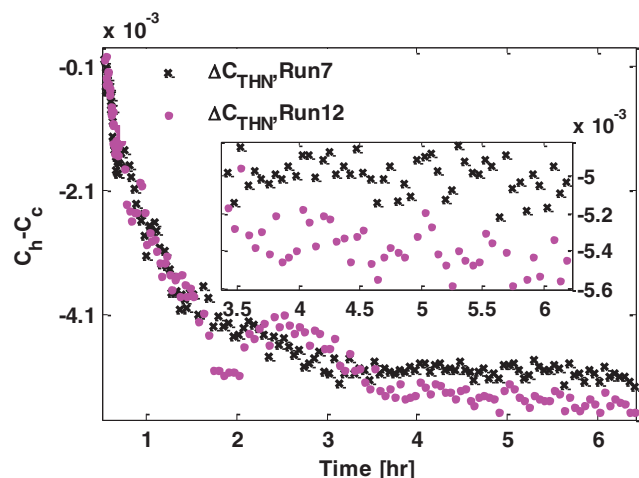


FIG. 6. Separation versus time during thermodiffusion phase of DSC-Run7 and 12-THN.

By adjusting the amplitudes of each laser and combining these obtained data with the values of the pure diffusion coefficients, it is possible to calculate D_{T1} and D_{T2} using Eq. (15). In this case, because the diffusion matrix of the mixture with this specific composition was not found in literature, these coefficients had to be estimated. Either the results of the diffusion stage of the experiment in an isothermal condition or curve-fitting using Eqs. (7) and (8) were used to calculate the coefficients. Thus, the calculation of the diffusion coefficients involved at least four to six unknown parameters that were estimated using curve-fitting methods.

V. DATA PROCESSING METHODOLOGY

The principal data analysis method that was used in this study was a combination of different Fourier transform techniques. As illustrated in Fig. 7, the procedure established for image processing was as follows: after downloading the raw data and converting both MR (Moveable Red Laser) and MN (Movable Near infrared Laser) binary files to digital bitmap images (see Figs. 7(a) and 7(b)), each interferogram was subjected to cropping either to separate the specific cell from the others or to remove crashed pixels around the walls. After post-processing of ODI result can be performed as follows.

A. Image processing procedure

As described earlier, there were two lasers with different wavelengths (670 nm and 935 nm) inside the moving bridge. The images that were taken by the laser with $\lambda = 670$ nm are called MR and those with $\lambda = 935$ nm are called MN. In the case of ternary systems, in each loop of image processing, four images must be taken simultaneously. Two references that remain without any change until the end of the process were employed to normalize the MR and MN images separately. See Figs. 7(c) and 7(e) which show representative MR and MN reference images, respectively. In addition to these two reference images, one MR and one MN image were processed in each loop as will be described later (Figs. 7(d) and 7(f)). Each image was then reconstructed by performing a two-dimensional (2D) Fourier transform of the fringe image, as illustrated in Figs. 7(g)–7(j). As shown in Figs. 7(k)–7(n), the images were processed by filtering a selected band of the spectrum that included one of the non-zero peaks, replacing this band at the middle of the spectrum, and performing an inverse 2D Fourier transform of the filtered result. A basic schematic of the rectangular band filter is given in Fig. 7(x). In this filter mask, white represents the maximum value one of the intensity and is used to filter the symmetrical band with respect to the x-axis. As the size of the filter mask decreased, the quality of the phase map increased and stronger noise reduction was achieved. However, there was a limitation for the size of this mask beyond which resulted in a crashed phase map by merging two continues phase bands together. The proper mask size varied between cases as a function of the maximum number of bands in the phase image. In this stage, an unwrapped phase of the intensity function was extracted, which possessed continuous values from $-\pi$ to $+\pi$.

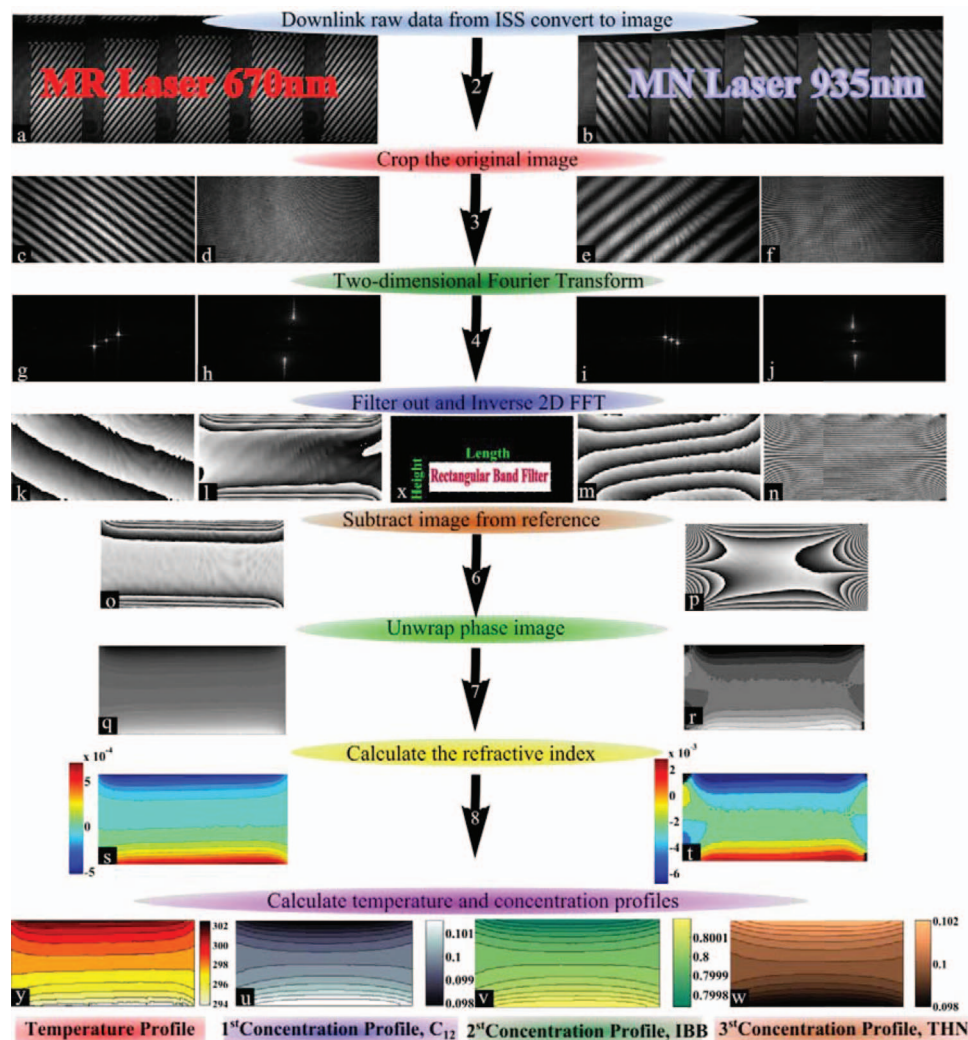


FIG. 7. Principle scheme of Fourier transform image processing technique to analyze optical digital interferometry of a ternary system: (a) and (b) Converted binary MR and MN lasers data to bitmap images, (c) and (e) cropped MR and MN reference images, respectively, (d) and (f) cropped current MR and MN images, respectively, (g)–(j) two-dimensional fast Fourier transform magnitude of image in parts (c), (d), (e), and (f), respectively, (k)–(n) inverted 2D fast Fourier transform magnitude of filtered image in parts (g), (h), (i), and (j), respectively, (o) and (p) subtracted MR and MN images from reference images, respectively, (q) and (r) unwrapped phase images, (s) and (t) refractive index profiles of MR and MN lasers, respectively, (u)–(w) concentration contours of C_{12} , IBB and THN, respectively, (x) filter mask to filter out one of the non-zero peaks, (y) temperature contour.

A similar procedure was applied to the reference images to evaluate $\phi_{ref}(x, y) = \phi(x, y, t_{ref})$. Next, reference images were used by subtracting the concurrent MR or MN image from the reference image, which resulted in a wrapped phase difference map. Thus, the required phase difference, $\Delta\phi$, or phase distribution, was given by the difference between the phase of the i th image and the reference image³¹

$$\Delta\phi(x, y, t_i) = \phi(x, y, t_i) - \phi_{ref}(x, y). \quad (12)$$

1. Phase unwrapping

Many fringe analysis techniques such as Fourier transform fringe analysis, phase stepping, and wavelet transform fringe analysis require the use of the arctangent function.⁵² In the case where there are no disturbances in the phase data, the unwrapped phase can be easily obtained by integrating the phase gradients over the whole data set, and this may be

performed in a manner that is independent of the actual integration path. However, if there are several sources of disturbances this simple unwrapping approach fails in the vast majority of cases.^{53,54} Current techniques for two-dimensional phase unwrapping can be roughly classified as either local or global phase unwrapping algorithms. A complete review of the two-dimensional phase unwrapping problem has been presented by Ghiglia and Pritt.⁵² All the algorithms are known to be robust but computationally intensive. As demonstrated in Fig. 8(a), the MATLAB built-in unwrap function or that of other general commercial software are not suitable for situations involving noise. This is due to the high sensitivity of these algorithms to crashed pixels, where even one can affect the rest of the field. This effect shows its influence along the vertical or horizontal line that includes the noisy pixel. Different complex approaches directly provide an accurate estimation of the unwrapped phase distribution from a noisy reconstructed interference field, thereby

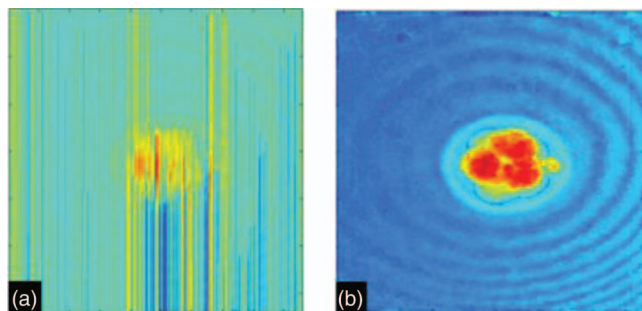


FIG. 8. Comparison between MATLAB and this study unwrap function, (a) unwrap using MATLAB's unwrap function, (b) unwrap method used in this study.⁵²

bypassing cumbersome and error-prone filtering and 2D phase unwrapping procedures.⁵⁵ In order to solve this problem, different methods are used, as illustrated in Fig. 8(b).⁵² Using our method results in a smooth field without any fluctuation or discrete value of phase because this method removed or minimized the influence of noise, which exist close to walls in the interferometry images. In this method, the pixel at the center of image was used as a reference pixel and was used to calculate the phase value for the neighboring pixels. The wrapped phase of a pixel was compared with a neighboring pixel that has been previously validated. If the difference between two neighbor pixels is less than π , the phase remained unchanged. The phase was changed to 2π plus its wrapped phase if the difference was less than $-\pi$. Finally, if the difference between the two pixels was more than π , the phase was equal to its wrapped phase minus 2π . At the end, a smooth 2D plot of phase change was obtained in the range $-\pi$ to π

$$\phi_{continuous}(x_j, y_i) = \phi(x_j, y_i) + 2\pi n(x_j, y_i), \quad i, j = 1, 2, \dots, \quad (13)$$

where i and j represent the coordinate index of pixels in the x and y directions, respectively, and m and n are the numbers of pixels in the x and y directions, respectively. For more details on this method, see the publication of Abdul-Rahman.⁵⁹

B. Calculation of the change in refractive index

The phase difference obtained by the described unwrap process was used to calculate $\Delta n(x, y)$, the distribution of the refractive index difference with respect to the reference image inside the cavity. This distribution allowed the calculation of the temperature and concentration variations in the cell as well as the difference between the hot and cold sides. The relation between phase difference $\Delta\phi$ and Δn is illustrated below in Eq. (14)

$$\Delta n(x, y) = n(x, y) - n_{ref}(x, y) = \frac{\lambda}{2\pi L} \Delta\phi(x, y), \quad (14)$$

where L is the optical path, i.e., the thickness of the liquid layer that the laser light passed through. From the above equation, the variation of refractive index was equivalent to the change of the optical phase.

When separation in the mixture has not reached the steady state, the aided genetic algorithm (GA) with fast robust

discretized smoothing can be implemented to find the curve that provides the best fit to the experimental separation.⁵¹ The GA method accurately estimates the Soret and diffusion coefficients simultaneously with a proper objective function. In a steady-state regime, an ideal case where time goes to infinity or reaches the diffusion time, the complex differential transient equations of separation can be simplified and the Soret coefficient can be calculated as follows:

$$S_{Ti} = \frac{\Delta C_{i,st}}{C_{i,0}(1 - C_{i,0})\Delta T}, \quad (15)$$

where $\Delta C_{i,st}$ is the stationary separation of component i , $C_{i,0}$ is the initial mass fraction of component i , and S_{Ti} represents the Soret coefficient of the i th component. Both runs lasted 6 h with the thermal gradient on. It must be noted that in ternary systems the summation of all three Soret coefficients is not equal to zero.

C. Data smoothing

Data smoothing techniques were used to eliminate noise from the plot of maximum refractive index variation versus time. As shown in Fig. 9, there are some outlying data points in the refractive index as a result of noise in a few images during the Fourier transform process. Using a data smoothing function, a best-fit curve is drawn. The fit was called the "Smooth," while the residuals were called the "Rough." These relate to the experimental data as follows:

$$\text{Data}_{\text{Experimental}} = \text{Data}_{\text{Smooth}} + \text{Data}_{\text{Rough}}. \quad (16)$$

The Rough was the sum of additive noise from a symmetric distribution with a mean value of zero and a certain variance or discontinuous noise.⁵⁰ In this paper, a fast, robust version of a discretized smoothing spline was used.⁵¹ This method, based on a Discrete Cosine Transform (DCT), allowed robust smoothing of equally spaced data in one and higher dimensions. The accuracy of this model has been illustrated using MATLAB.⁵¹

D. Genetic algorithm

After applying the robust smoothing method to the experimental data points, Eqs. (7) and (8) can be used to estimate

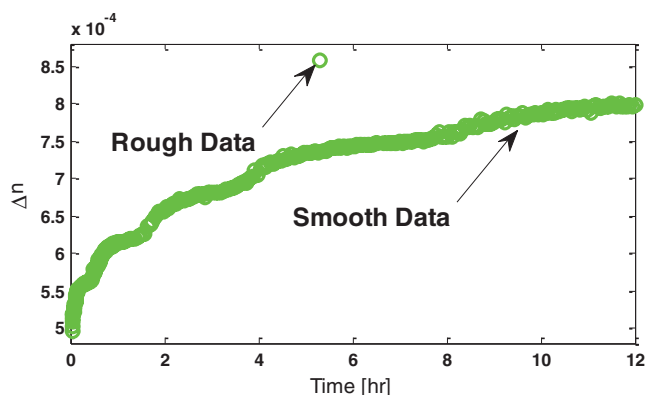


FIG. 9. 312 data points of refractive index versus time on MR laser.

S_T and D simultaneously by implementing the GA. In this case, there were more than four free parameters to be evaluated and corrected at each iteration of solving the curve-fitting problem. The positive or negative sign of the Soret coefficients in Eqs. (7) and (8) showed the direction of separation of each component either toward the hot or cold sides of the cell.

During the first ten minutes of the experiment, the separation of components was very small, and the influence of noise caused fluctuations in the separation. Thus, if the objective function was linearly related to the maximum separation in the field, it will severely affect the final solution. Moreover, as long as the separation value approaches steady state condition, the maximum separation between the hot and cold sides must have greater influence on the objective function. Thus, the objective function must be a function of time in the form of the least square error function

$$Err = \sum_{i=1}^n \left[\frac{1}{n} (t + \tau_D) (C_{exp} - C_{curve})^2 \right], \quad (17)$$

where n is the number of images, and t is the time used to intensify the influence of each data point according to the time at which the data are recorded. Using diffusion time τ_D in the objective function causes a linear variation between the first and the last datum such that the effect on the objective function of the last image is two times larger than the effect of the first. Finally, C_{exp} is the experimental concentration, and C_{curve} represents the current fitted curve.

E. Experimental accuracy, calculation of temperature and concentration profiles

1. Accuracy of the experiment

Concentration and temperature contribute to the variation of refractive index for any given wavelength based on the relationships that are given in Eqs. (10) and (11). During the first stage of the experiment when there was no temper-

ature difference, no refractive index variation should be observed; however, because of noise in the optical system, some fluctuations with a mean value of zero are recorded. These fluctuations present a possible error in the measurement. As shown in Fig. 10, the maximum refractive index variation between the hot and cold walls was less than 2×10^{-5} for the MN laser and less than 1×10^{-5} for the MR laser at isothermal conditions. This means that the maximum error in measurement of temperature variations is smaller than 0.08 K for the MN laser, while the MR laser shows a better and more accurate performance with the maximum error less than 0.04 K.

2. Temperature profile

Because thermal time was noticeably smaller than diffusion time (about 6 h in this case), ignoring a few minutes at the beginning of the experiment may not change the final concentration profile at the end of diffusion time. Consequently, during the first thermal time Eqs. (10) and (11) can be rewritten as follows:

$$\Delta T(x, y) = \frac{\Delta n_1(x, y)}{\left(\frac{\partial n_1}{\partial T} \right)_{T_0, C_0, \lambda_1}}, \quad (18)$$

$$\Delta T(x, y) = \frac{\Delta n_2(x, y)}{\left(\frac{\partial n_2}{\partial T} \right)_{T_0, C_0, \lambda_2}}. \quad (19)$$

Accordingly, the temperature profile in the system can be measured with both lasers separately.

3. Concentration profile

According to the theory of heat transfer in a liquid system, the temperature profile will not change after the first thermal time. Consequently, after that time any derivative of temperature is equal to zero and Eqs. (10) and (11) can be

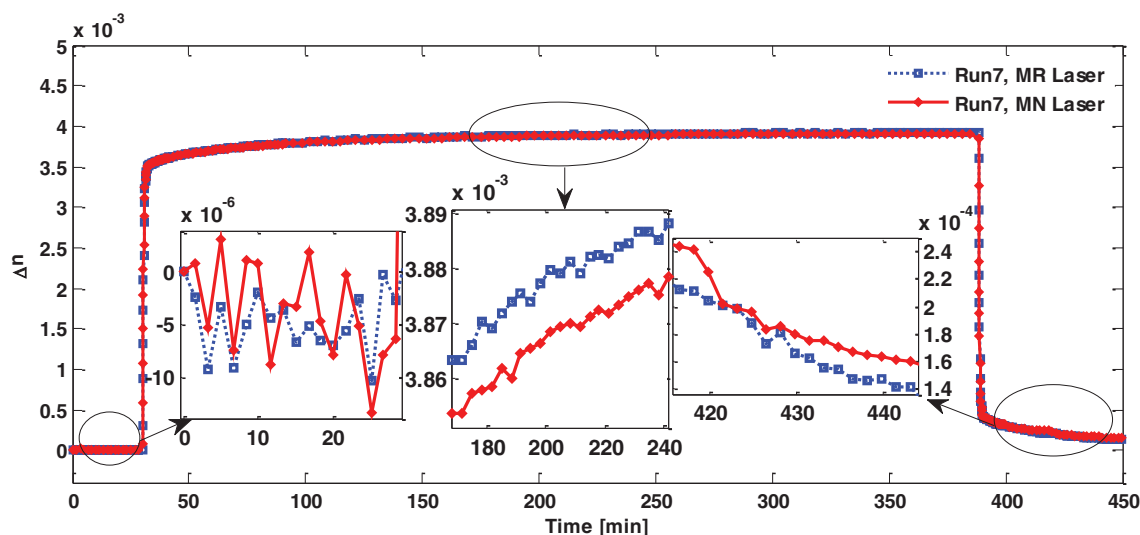


FIG. 10. Refractive index difference between hot and cold walls versus time during isothermal, thermal, and diffusion conditions.

TABLE II. Optical properties of the THN-IBB-C₁₂ mixture measured at T = 298 K.⁵⁸

Laser type	$c_{o,THN}$ (wt.%)	$c_{o,IBB}$ (wt.%)	$c_{o,C_{12}}$ (wt.%)	λ (nm)	$(\partial n/\partial T)_{p,IBB,THN}$ / $10^{-4}(\text{K}^{-1})$	$(\partial n/\partial c_{C_{12}})_{p,T,THN}$ / 10^{-2}	$(\partial n/\partial c_{THN})_{p,T,IBB}$ / 10^{-1}	$(\partial n/\partial c_{IBB})_{p,T,C_{12}}$ / 10^{-2}
MR	10%	80%	10%	670	-4.812	-5.72	1.213	-7.57
MN	10%	80%	10%	935	-4.763	-5.38	1.240	-6.96

rewritten as follows:

$$\Delta n_1(x, y) = \left(\frac{\partial n_1}{\partial c_1} \right)_{T_0, C_2, \lambda_1} \Delta C_1(x, y) + \left(\frac{\partial n_1}{\partial c_2} \right)_{T_0, C_1, \lambda_1} \Delta C_2(x, y), \quad (20)$$

$$\Delta n_2(x, y) = \left(\frac{\partial n_2}{\partial c_1} \right)_{T_0, C_2, \lambda_2} \Delta C_1(x, y) + \left(\frac{\partial n_2}{\partial c_2} \right)_{T_0, C_1, \lambda_2} \Delta C_2(x, y). \quad (21)$$

So, the mass fraction of the first two components can be calculated as follows:

$$\begin{pmatrix} \Delta C_1(x, y) \\ \Delta C_2(x, y) \end{pmatrix} = \begin{pmatrix} \left(\frac{\partial n_1}{\partial c_1} \right)_{T_0, C_2, \lambda_1} & \left(\frac{\partial n_1}{\partial c_2} \right)_{T_0, C_1, \lambda_1} \\ \left(\frac{\partial n_2}{\partial c_1} \right)_{T_0, C_2, \lambda_2} & \left(\frac{\partial n_2}{\partial c_2} \right)_{T_0, C_1, \lambda_2} \end{pmatrix}^{-1} \times \begin{pmatrix} \Delta n_1(x, y) \\ \Delta n_2(x, y) \end{pmatrix}. \quad (22)$$

The contrast factors for $\lambda = 670$ nm and $\lambda = 935$ nm at the mean temperature of 298 K are provided in Table II.

VI. RESULTS AND DISCUSSION

In this study, several parameters such as refractive index, temperature, and concentration fields in the cavity were studied in detail. Digital optical interferometry provided a large view over the entire cell and allowed the identification of the convection-free zones as well as the temperature and concentration distributions in the cell. The main objective of this paper is not only to determine the separation of the components in the cell and measure the Soret coefficients, but also to study the quality of the SODI-DSC apparatus during the thermal and mass diffusion times to determine the accuracy of their measurement of thermodiffusion. For this purpose, the behavior of the mixture was studied close to both the hot and cold walls inside the cavity at different locations and as a function of time.

A. Refractive index variation

Figure 10 shows the maximum refractive index variation between the hot and cold walls. The similarity between the red and blue lines in the plot shows that the MN and MR lasers provided consistent data. In addition, if one considers the mentioned similar behavior of lasers in Fig. 10 and the

slight differences in the contrast factors between these two lasers, it can be understood that separation in the ternary system of the SODI experiment can be extracted hardly. On the other hand, because of the high precision of the measurements in this optical method and using an advance post-processing techniques here, we could analyze the refractive index differences accurately (see magnified plots at the center of Fig. 10). It must be noted that although this difference was well identified during the thermodiffusion phase, after removing the temperature gradient there were more fluctuations that prevented having smooth curves of refractive index variations, especially at times such as the period between 420 min and 430 min. This conflict results in large variations in the calculated concentration distributions.

B. Temperature variation

A linear variation in the thermal gradient was reached in the cavity at the end of the thermal time. Liquid properties and the contrast factor at the mean temperature of 298 K were used to extract the temperature profile in the cavity at each pixel of the image (presented in Table II). The image yielded more than 1×10^6 data points across the cavity, which has a side area of 0.5 mm². It is vital to consider the separation as soon as a linear temperature gradient is achieved between the two walls. Figure 11 shows the mean temperature near the top and bottom walls during 120 s (before applying the temperature gradient, ΔT is applied at $t = 1820$ s) until the end of thermal time $t = 2000$ s.

When calculating the temperature field in the cavity experimentally, there were a number of notable points. First, the maximum temperature variation between the hot and cold

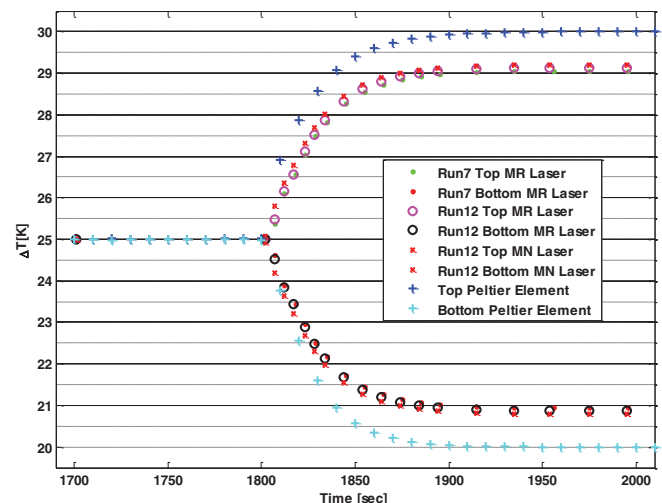


FIG. 11. Temperature difference between hot and cold sides during thermal time.

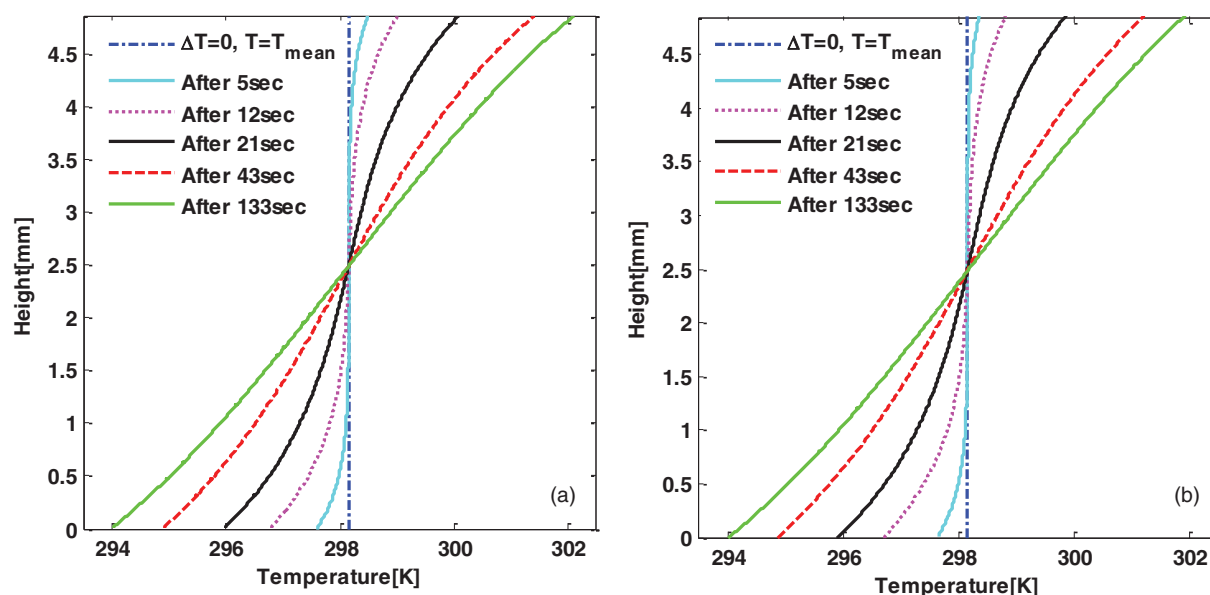


FIG. 12. Temperature variation between hot and cold walls of (a) Run7 and (b) Run12.

walls was 8.3 K in both Run7 and Run12, but the Peltier elements inside the copper plates of the cell array recorded a 10 K difference using the thermal controller system of the apparatus. This difference resulted from cropping of the images. Cropping the initial images removed the regions where the liquid was in contact with the copper blocks. In these removed areas, the optical signals were damaged by a defective alignment of the experimental cell with the optical axis of the interferometer, yielding reflection of the laser beam from the metal surface.⁵⁸ In this study, 5% of the pixels that were close to the top and bottom sides of the cavity were removed. Even so, with a linear variation of temperature at the end of one thermal time should have a temperature difference of about 9 K over 90% of the height of the cavity, contrasting the 8.3 K measured in the system. Thus, using the Peltier elements to measure the Soret effect might provide underestimated Soret coefficients, because the maximum separation is a strong function of the temperature gradient. Moreover, it can be observed that the MR and MN lasers in both cases provided their temperature results versus time with less than a 0.07 K

difference. This shows a high accuracy and repeatability of the thermal part of the SODI-DSC experiments if all properties of the mixture are optically measured. The maximum error in the temperature variation measurement is smaller than 0.1 K for both wavelengths, showing that the accuracy of this experiment for both the stability of the temperature variation and its measurement.

Figure 12 shows that temperature variations along the direction of the thermal gradient and at the middle of the cavity occur at different times during the thermal-time period. After the thermal time, the curvature of temperature variation along the temperature gradient direction changes to a linear variation with a small deviation. The similarity of the curves show that identical behavior of the temperature variation occurred in the two runs. Figure 13 illustrates the temperature field inside the cell at different times. For other studies that develop theoretical Soret diffusion model for multicomponent mixtures based on numerical simulation, these temperature patterns must be considered and modeled for boundary conditions.^{27,56}

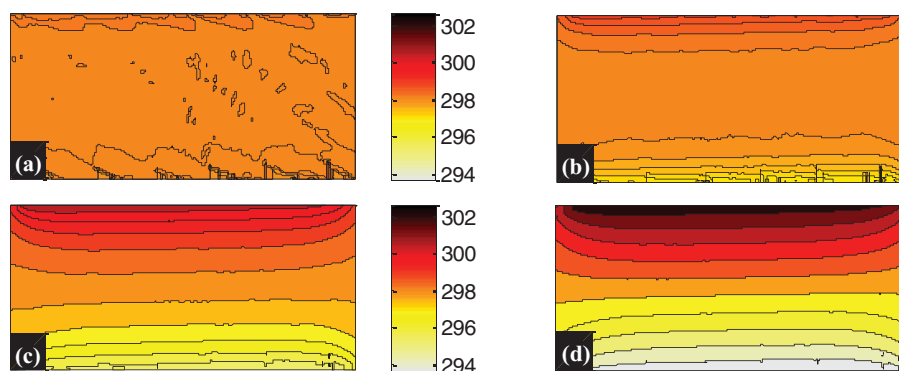


FIG. 13. Temperature distributions in the cavity at different times during thermal time, Run12 (a) after 1 s, (b) after 5 s, (c) after 41 s, and (d) after 133 s.

The approximate linear variation of the temperature in the cell between the cold and hot sides was also seen in the interference patterns, as shown in Fig. 13(d). Parts (a)–(c) illustrate the temperature field inside the cell at different times during the first thermal time. The temperature field within the liquid shows the temperature gradient induced the formation of convection in the liquid. This convection occurred because of heat fluxes close to the glass walls. These walls were supposed to provide thermal insulation for the sides of the cell. The lateral heat flux was also noticeable and clear in all phase images immediately after the thermal time (3 min after applying temperature), as shown in Fig. 14. These bands should be linear and parallel to the hot and cold walls; however, as a result of the heat fluxes the bands are not parallel. Close to the lateral walls and near the hot wall (upper half of the lateral walls), there was a gradient in the amount of heat transfer from the lower close to the wall to higher closer to the inside of the cell. Moreover, an opposite pattern of heat transfer was observed at the bottom half of the cavity close to the lateral wall, where the heat transfer gradient moves from high to low from the glass walls toward the middle of the cell. This means heat transferred from outside the cell near the lateral boundaries toward the middle of the cavity. Moreover, the point along the vertical walls where the gradient behavior from low to high changes to high to low is the only point with zero heat flux on the lateral wall. While this heat transfer did

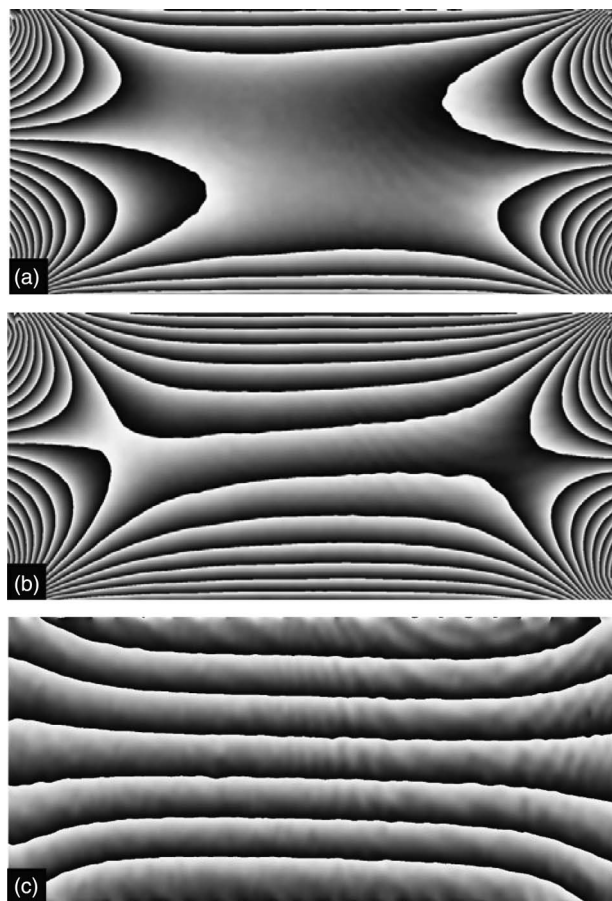


FIG. 14. Phase and phase difference distributions in the cavity at different times, Run12 (a) phase after 1 min, (b) phase after 6 h, and (c) phase difference of first and last phase.

not strongly affect the thermal performance of the apparatus at the center region of the cell, it is important for numerical analysis to consider that the cell did not have perfect thermal isolation close to the lateral walls. In order to measure the separation or concentration contour, it was required to crop the images and consider the region far from the areas where these heat fluxes induced small convection cells near the lateral boundaries.

The thermal conductivity of the O-rings that are shown in Fig. 5 caused the slight lateral deformation of the temperature field shown in Fig. 14. This effect had been observed in previous studies of the SODI project.^{28,29,35,37,39} From the internal side of the O-rings, the small gap between the copper and quartz was filled by the working liquid. On the external side, the gap was filled by the surrounding gas that acted as a poor heat conductor.^{28,29,35,37} Consequently, the largest thermal gradient arose at the corners, due to the relatively high heat conductivity of the rubber sealing and surrounding regions. This is shown in detail in Fig. 13(d).

C. Diffusion time and concentration profile

Taking the reference image at the end of thermal time (Fig. 14(a)) and subtracting the image at the end of the thermodiffusion phase (Fig. 14(b)), removed the influence of heat fluxes from the field (see Fig. 14(c)). On the other hand, a nonlinear phase map was produced because of the nonlinear temperature distribution at the corners, as shown in Fig. 14(c). This map shows some deviance from pure linear separation close to the lateral walls. In order to ignore this part of the cell in the Soret coefficient measurements, all images were re-cropped and processed such that only the middle part of the cell was considered for the estimation.

The maximum concentration difference, ΔC (i.e., the Soret separation) for the two cases can be extracted from the chart shown in Fig. 15. The smooth pattern of separation of THN toward the cold side of the cell versus time is characteristic of a positive Soret effect and is consistent in both Run7 and Run12. There was similar separation observed for IBB, although it separated toward the hot wall and showed a negative Soret effect. While there are some fluctuations in the

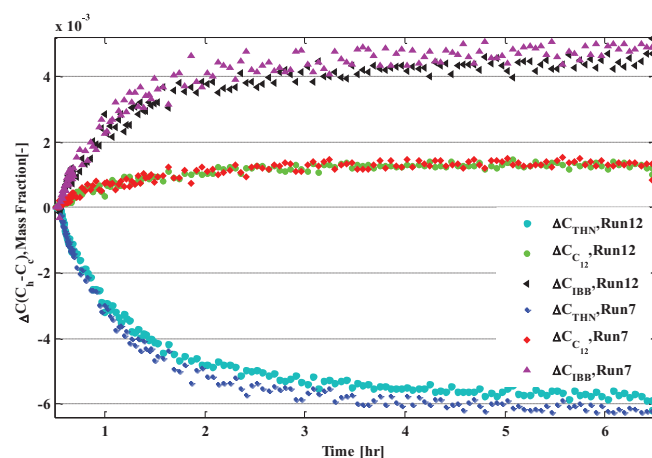


FIG. 15. Separation between hot and cold sides during thermodiffusion time.

TABLE III. SODI-DSC Runs7 and 12 experimental results with 10 K temperature gradient onboard ISS.

RUN#	$\Delta C_{\max}/10^{-3}(c_h - c_c)$			$\frac{\Delta c/10^{-3}}{c_0(1-c_0)\Delta T} _{t=6h} (K^{-1})$			Fitted $S_T/10^{-3}(K^{-1})$			$\Delta T_{\max}(K)$	
	THN	IBB	C ₁₂	THN	IBB	C ₁₂	THN	IBB	C ₁₂	MR	MN
Run7	-6.20	4.89	1.18	8.26	-3.65	-1.75	8.28	-3.71	-1.74	8.29	8.34
Run12	-5.89	4.70	1.32	7.86	-3.52	-1.79	8.19	-3.68	-1.82	8.33	8.37

separation of IBB in Run7 after 2 h in the thermodiffusion stage, the separation of C₁₂ behaved identically for both runs. The separation magnitude of both THN and IBB were similar, with the separation of THN being slightly stronger, as summarized in Table III. This means that the third component moves toward the hot side weakly. Despite this weaker separation of C₁₂, which can be barely detected by ODI, C₁₂ shows a negative thermodiffusion coefficient in this mixture at a mean temperature of 298 K. The similar values of the separation of the components for the two runs demonstrate the repeatability of digital optical interferometry not only to calculate Soret coefficients for binary systems, but also to measure the Soret coefficients in ternary systems.

Figures 16 and 17 show the concentration variations of THN and IBB, respectively, along the direction of the thermal gradient at the middle of the cavity at several times during the diffusion period in four runs. Despite the small amount of separation during the first hour of the thermodiffusion phase, the separation started close to the hot and cold walls with a linear separation variation from the top to the bottom of the cavity. This was observed in both runs. According to Figs. 16 and 17, after 4–5 h steady state separation was achieved. It can be concluded that the ISS provides enough thermodiffusion time in a suitable environment for this experiment.

The measurement of transport properties of ternary mixtures via ODI is highly sensitive to errors for a few reasons. First is the weak separation of one of the components. As a result of this small separation, a small processing error always arose. The second reason is the close performance and contrast factors of the MN and MR laser for this test mix-

ture, which required the use of a sensitive image processing procedure. The third is the image processing calculation error. In this study, one of the most accurate processing methods (windowed Fourier transform) was employed to analyze the experiment. But it is impossible to remove the calculation error for the component with separation close to zero in comparison with other components. The last reason is the quality of the images, which are not of as high a quality as those from the IVIDIL project, due to the presence of dust particles on the front glass disturbing a clear view of the cell.

Figures 18 and 19 show the concentration contours of THN and IBB, respectively, during the thermodiffusion time. Visible separation of THN was evident after 30 min; however, as Fig. 19(a) shows, there was a mostly uniform concentration of IBB in the field. Thus, IBB separation started later than that of THN. As discussed earlier, the separation started near the cold and hot walls, then later spreading to the regions away from those boundaries. Regardless of the weak amount of separation of THN and IBB during the first two hours of the experiments, there was noticeable separation of these two components later on, as shown in Figs. 18(d) and 19(b). Furthermore, it can be seen that far from the boundaries of the convection-free zone the condition of zero mass flux was satisfied at steady state. As shown in Table I, the lighter component moved toward the cold side. While the molecular mass of THN and IBB are close, the heavier one, IBB, experienced a separation toward the hot side and THN, which has an intermediate molecular mass, strongly separated toward the cold wall.

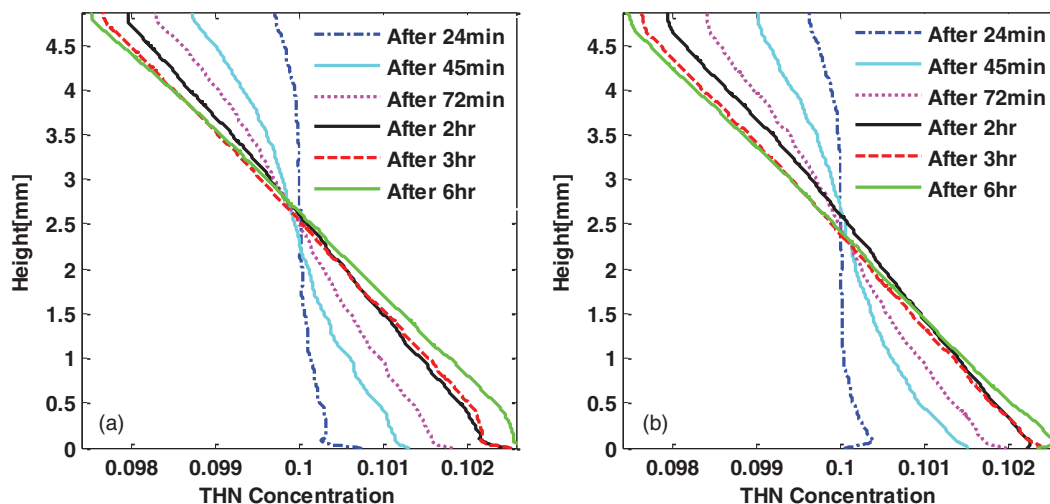


FIG. 16. THN concentration variation between hot and cold walls at various times, (a) Run7 and (b) Run12.

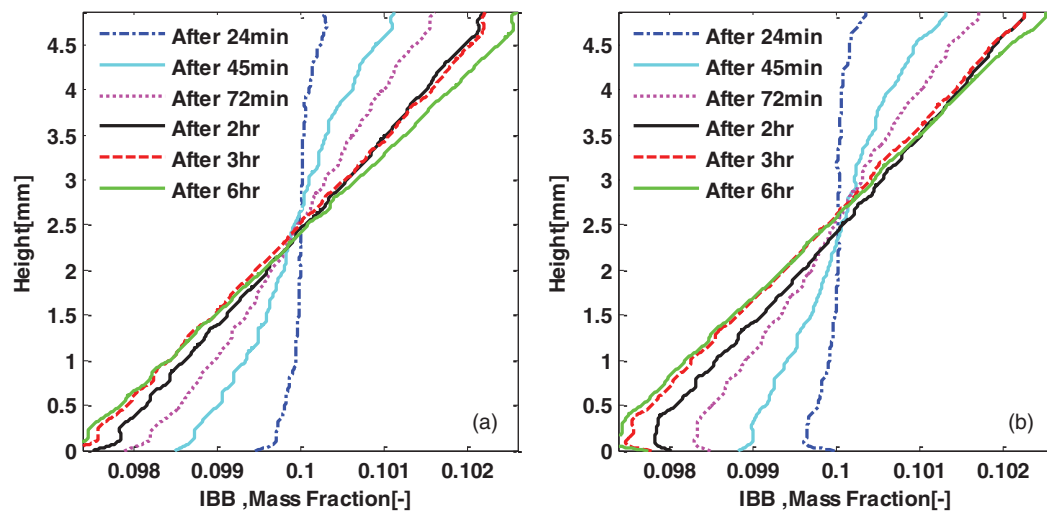


FIG. 17. IBB concentration variation between hot and cold walls at various times, (a) Run7 and (b) Run12.

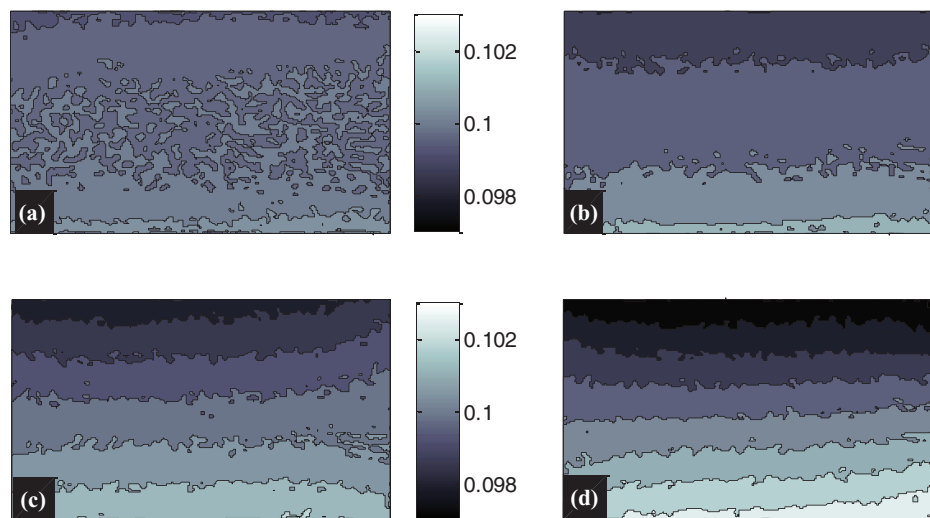


FIG. 18. THN concentration profiles in the cavity at different times during diffusion time, Run12 (a) after 30 min, (b) after 75 min, (c) after 3.5 h, and (d) after 6 h.

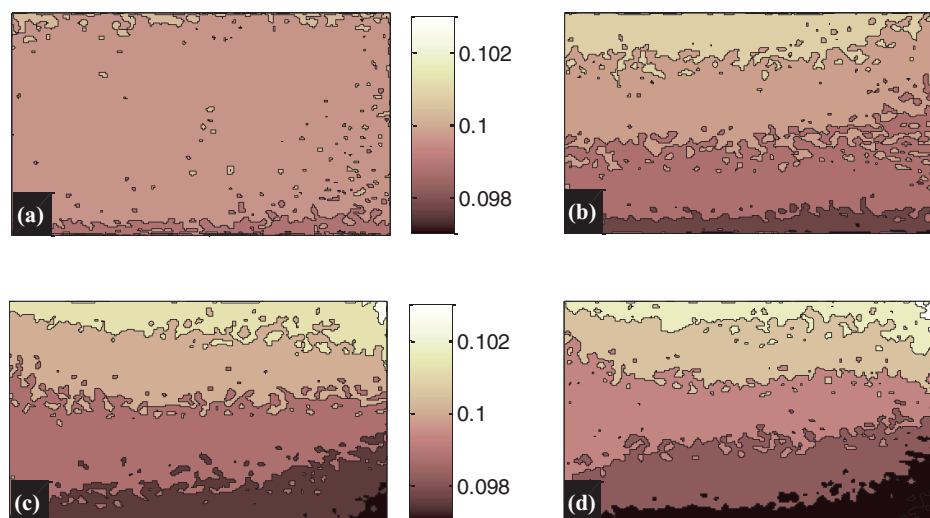


FIG. 19. IBB concentration profiles in the cavity at different times during diffusion time, Run12 (a) after 30 min, (b) after 75 min, (c) after 3.5 h, and (d) after 6 h.

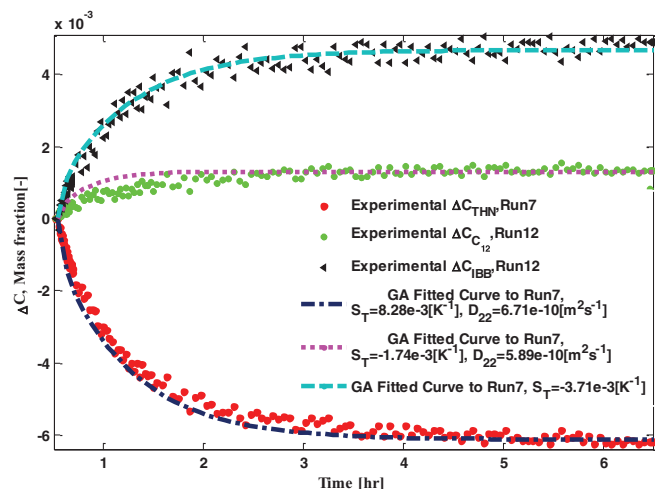


FIG. 20. Transient experimental separations of Run12, associated with best fitted curve.

D. Soret coefficient, S_T

In contrast with binary mixtures, there has been limited analysis done in cases in which multi-component mixtures are considered. According to the literature, this is the first time that Soret coefficients of this mixture with this specific composition have been reported. Thus, it is particularly interesting to compare the Soret coefficients as estimated via the GA algorithm with those obtained by the value from the steady-state separation. The values of the Soret coefficients, maximum separations, and other data for Run7 and Run12 for this test mixture are summarized in Table III. Both runs provided similar results with only marginal differences. However, the values of GA show a slightly greater value of S_T , which means that although the steady-state condition is reached; there is still a small ratio of separation of the components in the system. The average values of the Soret coefficients of THN, C_{12} , and IBB are determined as -8.24×10^{-3} , -1.88×10^{-3} , and -3.69×10^{-4} [1/K], respectively.

Comparing the GA results with temporal experimental data was performed and the results are shown for Run12 in Fig. 20. It can be seen that the curves coincide well, especially for THN and IBB, which have a noticeable separation trend. The good match between the GA curve and the temporal experimental data curve also shows the good performance of evolutionary optimization algorithm to estimate diffusion coefficients.

VII. CONCLUSION

The main goal of this research, which was to determine the Soret coefficients of THN-IBB- C_{12} mixture with initial mass fractions of 0.10, 0.80, and 0.10, respectively, was achieved. The accuracy and problems with the quality of the SODI-DSC apparatus on board the ISS have been discussed. For this purpose, data obtained in Run7 and Run12 of the SODI-DSC with an assigned 10 K temperature difference were analyzed in detail. Mathematical analyses by means of Fourier transform image processing and a curve-

fitting method using GA were employed to obtain results that show an accurate fitting result.

The collected experimental results of SODI-DSC showed a linear temperature field inside the cell, particularly in its central section, with slight deformation of the temperature field at the walls of the cell. These distortions were caused by convective disturbances due to inhomogeneous heating. It was found that measuring the temperature difference experimentally and with ODI has a direct effect on the calculated Soret coefficients due to different temperatures reported in those methods. Although there are some nonlinear behaviors in the temperature gradient at the corners of the field, they do not affect the linear temperature and separation variation at the center of the cell and along the thermal gradient. Thus, the result of the central region must be used to measure the Soret coefficients.

Six hours of thermodiffusion time are sufficient to reach steady-state separation of this particular mixture, including a barely noticeable amount of separation during the last three hours of the experiment. Results obtained by steady-state values appear to be comparable to those obtained by fitting the entire dynamics by means of a genetic algorithm estimating four free parameters. It must be noted that the heavier component (C_{12}) moves toward the hot side. While the molecular mass of THN and IBB are close, the heavier one, which is IBB, experienced the separation toward the hot side as well. Finally, THN with an intermediate molecular mass strongly separated toward the cold wall. This shows that the ODI not only allows measuring the diffusion coefficients in binary systems with high precision, but it also can be used to analyze multi-component systems. Reaching this goal requires employing different lasers not only with different wavelengths but also with different contrast factors on the test mixture. Using two lasers with mostly similar properties corresponding to the test mixture was the main point that provided difficulties in processing the results. Moreover, the entire calculation was a function of the accurate measurement of the contrast factors. In summary, the ISS provided a suitable environment for this experiment and the SODI-DSC results of cell number two were found to be clear and reliable.

ACKNOWLEDGMENTS

The authors would like to acknowledge the Canadian Space Agency (CSA) and the Natural Sciences and Engineering Research Council of Canada (NSERC) for funding this work. In addition, we appreciate great reviewer's comments that made this work stronger.

NOMENCLATURE

Δn	=	change in refractive index
ΔC	=	maximum concentration difference
ΔT	=	maximum temperature difference [K]
i, j	=	coordinate index of pixel
$c_{0,i}$	=	initial concentration of i th component
T	=	temperature [K]
L	=	optical path of the cell [mm]
$\Delta \phi$	=	phase distribution

$\left(\frac{\partial n}{\partial T}\right)$	= thermal contrast factor [K^{-1}]
$\left(\frac{\partial n}{\partial C}\right)$	= concentration contrast factor
t	= time [s, min, h]
τ_{th}	= thermal relaxation time [s]
τ_c	= diffusion relaxation time [h]
T_h	= temperature at the hot side of the cavity [K]
T_c	= temperature at the cold side of the cavity [K]
D	= molecular diffusion coefficient [$m^2 s^{-1}$]
D_T	= thermodiffusion coefficient [$m^2 s^{-1} K^{-1}$]
S_T	= Soret coefficient [K^{-1}]
C_c	= concentration at the cold wall [mass fraction]
C_h	= concentration at the hot wall [mass fraction]
λ	= laser wavelength [nm]
χ	= thermal diffusivity
x,y	= Cartesian co-ordinates in a 2D plane

Subscript

exp	= experimental
h	= hour
min	= minute
Ref	= reference
th	= thermal
st	= steady

- ¹M. Touzet, G. Galliero, V. Lazzeri, M. Z. Saghir, F. Montel, and J. Legros, *C. R. Méc.* **339**, 318–323 (2011).
- ²O. Thomas, Ph.D. dissertation, Stanford University, 2007.
- ³S. Srinivasan, M. Eslamian, and M. Z. Saghir, Paper No. IAC-09-A2.3.1 (IAC, 2009).
- ⁴M. Eslamian and M. Z. Saghir, *Phys. Rev. E* **80**, 011201 (2009).
- ⁵K. Ghorayeb and A. Firoozabadi, *Soc. Pet. Eng. J.* **5**, 158 (2000).
- ⁶C. G. Jiang, M. Z. Saghir, M. Kawaji, and K. Ghorayeb, *Int. J. Therm. Sci.* **43**, 1057–1065 (2004).
- ⁷S. Srinivasan, M. Demek, and M. Z. Saghir, *Int. J. Therm. Sci.* **49**, 1613 (2010).
- ⁸M. Chacha and M. Z. Saghir, *Int. J. Therm. Sci.* **44**, 1–10 (2005).
- ⁹A. Ahadi and M. Z. Saghir, *Fluid Dyn. Mater. Process.* **287**, 1–26 (2012).
- ¹⁰J. K. Platten, M. M. Bou-Ali, and J. F. Dutrieux, *J. Phys. Chem. B* **107**, 11763–11767 (2003).
- ¹¹J. K. Platten, M. M. Bou-Ali, P. Costesque, J. F. Dutrieux, W. Koehler, C. Leppla, S. Wiegand, and G. Wittko, *Philos. Mag.* **83**, 1965–1971 (2003).
- ¹²H. Nasrabadi, H. Hoteit, and A. Firoozabadi, *Transp. Porous Media* **67**, 473–486 (2007).
- ¹³J. P. Naumann, A. Martin, H. Kriegs, M. Larrañaga, M. M. Bou-Ali, and S. Wiegand, *J. Phys. Chem. B* **116**, 13889–13897 (2012).
- ¹⁴P. Blanco, M. M. Bou-Ali, J. K. Platten, D. A. d. Mezquia, J. A. Madariaga, and C. Santamaria, *J. Chem. Phys.* **132**, 114506 (2010).
- ¹⁵Y. Yan, P. Blanco, M. Z. Saghir, and M. M. Bou-Ali, *J. Chem. Phys.* **129**, 194507 (2008).
- ¹⁶M. Marucci, S. Pettersson, G. Ragnarsson, and A. Axelsson, *J. Phys. D* **40**, 2870 (2007).
- ¹⁷F. Croccolo, H. Bataller, and F. Scheffold, *J. Chem. Phys.* **137**, 234202 (2012).
- ¹⁸P. N. Segrè, R. Schmitz, and J. V. Sengers, *Physica A* **195**, 31 (1993).
- ¹⁹C. Leppla and S. Wiegand, *Philos. Mag.* **83**, 1989–1999 (2003).
- ²⁰A. Perronace, C. Leppla, F. Leroy, B. Rousseau, and S. Wiegand, *J. Chem. Phys.* **116**, 3718–3729 (2002).
- ²¹W. Koehler, *J. Chem. Phys.* **98**, 660–668 (1993).
- ²²T. Pollak and W. Koehler, *J. Chem. Phys.* **130**, 124905 (2009).
- ²³A. Koniger, H. Wunderlich, and W. Koehler, *J. Chem. Phys.* **132**, 174506 (2010).
- ²⁴W. Koehler, A. Koniger, and B. Meier, *Philos. Mag.* **89**, 907–923 (2009).
- ²⁵X. Zhong, *J. Opt. A: Pure Appl. Opt.* **8**, 617 (2006).
- ²⁶K. M. Yassien, *J. Opt. A: Pure Appl. Opt.* **11**, 075701 (2009).
- ²⁷V. Shevtsova, T. Lyubimova, Z. Saghir, D. Melnikov, Y. Gaponenko, V. Sechenyh, J. C. Legros, and A. Mialdun, *J. Phys.: Conf. Ser.* **327**, 012031 (2011).
- ²⁸A. Mialdun and V. Shevtsova, *Microgravity Sci. Technol.* **21**, 31–36 (2009).
- ²⁹A. Mialdun and V. Shevtsova, *C. R. Méc.* **339**, 362–368 (2011).
- ³⁰A. Mialdun and V. M. Shevtsova, *Int. J. Heat Mass Transfer* **51**, 3164 (2008).
- ³¹A. Mialdun and V. Shevtsova, *J. Chem. Phys.* **134**, 044524 (2011).
- ³²M. Eslamian and M. Z. Saghir, *J. Non-Equilib. Thermodyn.* **34**, 97–131 (2009).
- ³³S. VanVaerenbergh, S. Srinivasan, and M. Z. Saghir, *J. Chem. Phys.* **131**, 114505 (2009).
- ³⁴S. Srinivasan and M. Z. Saghir, *Int. J. Therm. Sci.* **50**, 1125–1137 (2011).
- ³⁵V. Shevtsova, A. Mialdun, D. Melnikov, I. Ryzhkov, Y. Gaponenko, Z. Saghir, T. Lyubimova, and J. C. Legros, *C. R. Méc.* **339**, 310 (2011).
- ³⁶V. Shevtsova, D. Melnikov, A. Mialdun, and J. Legros, *Microgravity Sci. Technol.* **18**, 38–41 (2006).
- ³⁷V. Shevtsova, *Adv. Space Res.* **46**, 672–679 (2010).
- ³⁸V. Shevtsova, D. Melnikov, J. C. Legros, Y. Yan, Z. Saghir, T. Lyubimova, G. Sedelnikov, and B. Roux, *Phys. Fluids* **19**, 017111 (2007).
- ³⁹M. Lappa, SODI - Experiment Report 2 “Mission Operations Implementation Concept” (2011).
- ⁴⁰A. Mialdun, I. I. Ryzhkov, D. E. Melnikov, and V. Shevtsova, *Phys. Rev. Lett.* **101**, 084501 (2008).
- ⁴¹A. Mialdun, V. Yasnou, V. Shevtsova, A. Koniger, W. Koehler, D. A. de Mezquia, and M. M. Bou-Ali, *J. Chem. Phys.* **136**, 244512 (2012).
- ⁴²K. Shukla and A. Firoozabadi, *Ind. Eng. Chem. Res.* **37**, 3331–3342 (1998).
- ⁴³V. Shevtsova, Y. Gaponenko, D. Melnikov, I. Ryzhkov, and A. Mialdun, *Acta Astronaut.* **66**, 166 (2010).
- ⁴⁴A. Parsa and M. Z. Saghir, *ASME Conference Proceedings* (ASME/JSME 2011 8th Thermal Engineering Joint Conference, Honolulu, Hawaii, 2011), pp. T10024-1–T10024-5.
- ⁴⁵A. Parsa, S. Srinivasan, and M. Z. Saghir, “Impact of density gradients on the fluid flow inside a vibrating cavity subjected to Soret effect,” *Can. J. Chem. Eng.* **91**(3), 550–559 (2013).
- ⁴⁶S. Srinivasan and M. Z. Saghir, *J. Chem. Phys.* **131**, 124508 (2009).
- ⁴⁷A. Mialdun, C. Minetti, Y. Gaponenko, V. Shevtsova, and F. Dubois, *Microgravity Sci. Technol.* **25**(1), 83–94 (2013).
- ⁴⁸G. Wittko and W. Koehler, *Philos. Mag.* **83**, 1973–1987 (2003).
- ⁴⁹S. Mazzoni, SCI-ESA-HSO-ESR-DSC, ESA Unclassified Report #1, “DSC as part of the DCMIX project, Experiment Scientific Requirements” (European Space Research and Technology Centre, 2011).
- ⁵⁰J. W. Tukey, *Exploratory Data Analysis* (Addison-Wesley Publishing Company, 1977).
- ⁵¹D. Garcia, *Comput. Stat. Data Anal.* **54**, 1167–1178 (2010).
- ⁵²D. C. Ghiglia, M. D. Pritt, *Two-Dimensional Phase Unwrapping: Theory, Algorithms, and Software* (Wiley, 1998).
- ⁵³M. Hipp, J. Woisetschlager, P. Reiterer, and T. Neger, *Measurement* **36**, 53–66 (2004).
- ⁵⁴S. Li, X. Su, W. Chen, and L. Xiang, *J. Opt. Soc. Am. A* **26**, 1195–1201 (2009).
- ⁵⁵S. S. Gorthi and P. Rastogi, *Meas. Sci. Technol.* **20**, 075307 (2009).
- ⁵⁶ESA Scientific report. V. Shevtsova, M. Z. Saghir, T. Lyubimova, D. Melnikov, A. Mialdun, and R. Ilya, “1-year post-flight science report#1: influence of vibrations on diffusion in liquids (IVIDIL),” 2011.
- ⁵⁷Canadian Space Agency, “SODI-IVIDIL experiment report,” Report No. 1, 2010.
- ⁵⁸Q. Galand, Ph.D. dissertation, University De Bruxelles, Ecole Polytechnique De Bruxelles, 2012.
- ⁵⁹H. Abdul-Rahman, Ph.D. dissertation, Liverpool John Moores University, 2007.